Article

Sunlight-powered sustained flight of an ultralight micro aerial vehicle

https://doi.org/10.1038/s41586-024-07609-4

Received: 29 January 2024

Accepted: 23 May 2024

Published online: 17 July 2024

Check for updates

Wei Shen[1,5], Jinzhe Peng[1,5], Rui Ma[1], Jiaqing Wu[1], Jingyi Li[1], Zhiwei Liu[1,2,3,4], Jiaming Leng[2], Xiaojun Yan[1,2,3,4]✉ & Mingjing Qi[1,2,3,4]✉

Limited flight duration is a considerable obstacle to the widespread application of micro aerial vehicles (MAVs)[1–3], especially for ultralightweight MAVs weighing less than 10 g, which, in general, have a flight endurance of no more than 10 min (refs. 1,4). Sunlight power[5–7] is a potential alternative to improve the endurance of ultralight MAVs, but owing to the restricted payload capacity of the vehicle and low lift-to-power efficiency of traditional propulsion systems, previous studies have not achieved untethered sustained flight of MAVs fully powered by natural sunlight[8,9]. Here, to address these challenges, we introduce the CoulombFly, an electrostatic flyer consisting of an electrostatic-driven propulsion system with a high lift-to-power efficiency of 30.7 g W^{-1} and an ultralight kilovolt power system with a low power consumption of 0.568 W, to realize solar-powered sustained flight of an MAV under natural sunlight conditions (920 W m^{-2}). The vehicle's total mass is only 4.21 g, within 1/600 of the existing lightest sunlight-powered aerial vehicle[6].

There are numerous potential demands for micro aerial vehicles (MAVs), such as communication[10], environmental rescue[11] and monitoring[3,12]. However, existing MAVs suffer from short endurance. This problem is exacerbated for ultralight MAVs as they decrease in size[1–3], particularly those weighing less than 10 g, which often have a flight time of less than 10 min (refs. 1,4). For instance, a commercial centimetre quadrotor weighing 7 g (SKEYE Pico; https://trndlabs.com/pages/drone-academy_skeye-pico-drone) has a flight time of only 7 min, and an electromagnetic flapping-wing MAV weighing 3.1 g (DelFly Micro[13]) has a flight time of only 3 min (ref. 1). Traditional MAVs generally use electromagnetic motors as actuators. As the size of the vehicle decreases, the efficiency of electromagnetic motors decreases substantially owing to increased friction and resistive losses[3,14], resulting in low lift-to-power efficiencies. To achieve untethered and sustained flight for ultralight aerial vehicles, different types of actuator (such as piezoelectric ceramics[8,15,16], dielectric elastomers[17,18] and linear electromagnetic actuators[19,20]) have been used in previous studies to make lighter propulsion systems with higher efficiency, but large and bulky additional ground power systems (such as laser[21], high-intensity light[8] and wireless radio frequency[22]) are still needed to take off, which seriously hinders their practical applications.

Sunlight, as an ideal external energy source[6,9], is sustainable and widely available. It allows vehicles to travel without limitations by the ground power systems and can remarkably increase their flight endurance and cruising range[23]. Unfortunately, until now, no sunlight-powered MAV has been capable of achieving untethered sustained flight. This is due to the sharp decrease in energy conversion efficiency and lift-to-power efficiency of propulsion systems with existing driving approaches, such as electromagnetic motors, as the vehicle size decreases.

Here, to address the issues above, we introduce an electrostatic-driven propulsion system and an ultralight kilovolt onboard power system with low power consumption and high lift-to-power efficiency. Furthermore, we develop an ultralight, sunlight-powered MAV (CoulombFly), as shown in Fig. 1a, that achieves untethered sustained flight under natural sunlight. There are four notable advancements in this work. (1) Fully sunlight-powered sustained flight demonstration of MAVs (Fig. 1). (2) Design of an electrostatic motor for untethered flight (Fig. 2) and a high-voltage power converter (HVPC) generating 9-kV maximum output voltage within 1.13 g (Fig. 3). (3) Size reduction from the metre level (2 m) to the centimetre level (20 cm) and weight reduction from 2.60 kg to 4.21 g, for, to our knowledge, the world's smallest and lightest sunlight-powered rotorcraft[6] (Fig. 4a). (4) Development of a millimetre-sized (8 mm in diameter and 9 mg in mass) prototype for further miniaturization (Fig. 4b,c).

Vehicle design and sunlight-powered flight test

As shown in Fig. 1a, the 4.21-g sunlight-powered ultralight MAV mainly consists of an electrostatic-driven propulsion system (an electrostatic motor and a propeller) and an ultralight kilovolt power system (a HVPC and solar cells). The detailed parameters for the vehicle components are listed in Extended Data Table 1. The solar cells generate low d.c. voltage in natural sunlight conditions. The HVPC converts the low d.c. voltage (4.50 V) to a high d.c. voltage (9 kV) through a transformer with a 1:50 ratio and a 12-stage voltage multiplier. The high d.c. voltage is applied to the electrode plate of the electrostatic motor, creating a high-voltage electric field and driving the rotor to rotate, thus generating torque to drive the propeller for lift generation. The solar cells were placed some distance below the electrostatic

[1]School of Energy and Power Engineering, Beihang University, Beijing, China. [2]Collaborative Innovation Center of Advanced Aero-Engine, Beijing, China. [3]National Key Laboratory of Science and Technology on Aero-Engine Aero-Thermodynamics, Beijing, China. [4]Beijing Key Laboratory of Aero-Engine Structure and Strength, Beijing, China. [5]These authors contributed equally: Wei Shen, Jinzhe Peng. ✉e-mail: yanxiaojun@buaa.edu.cn; qimingjing@buaa.edu.cn

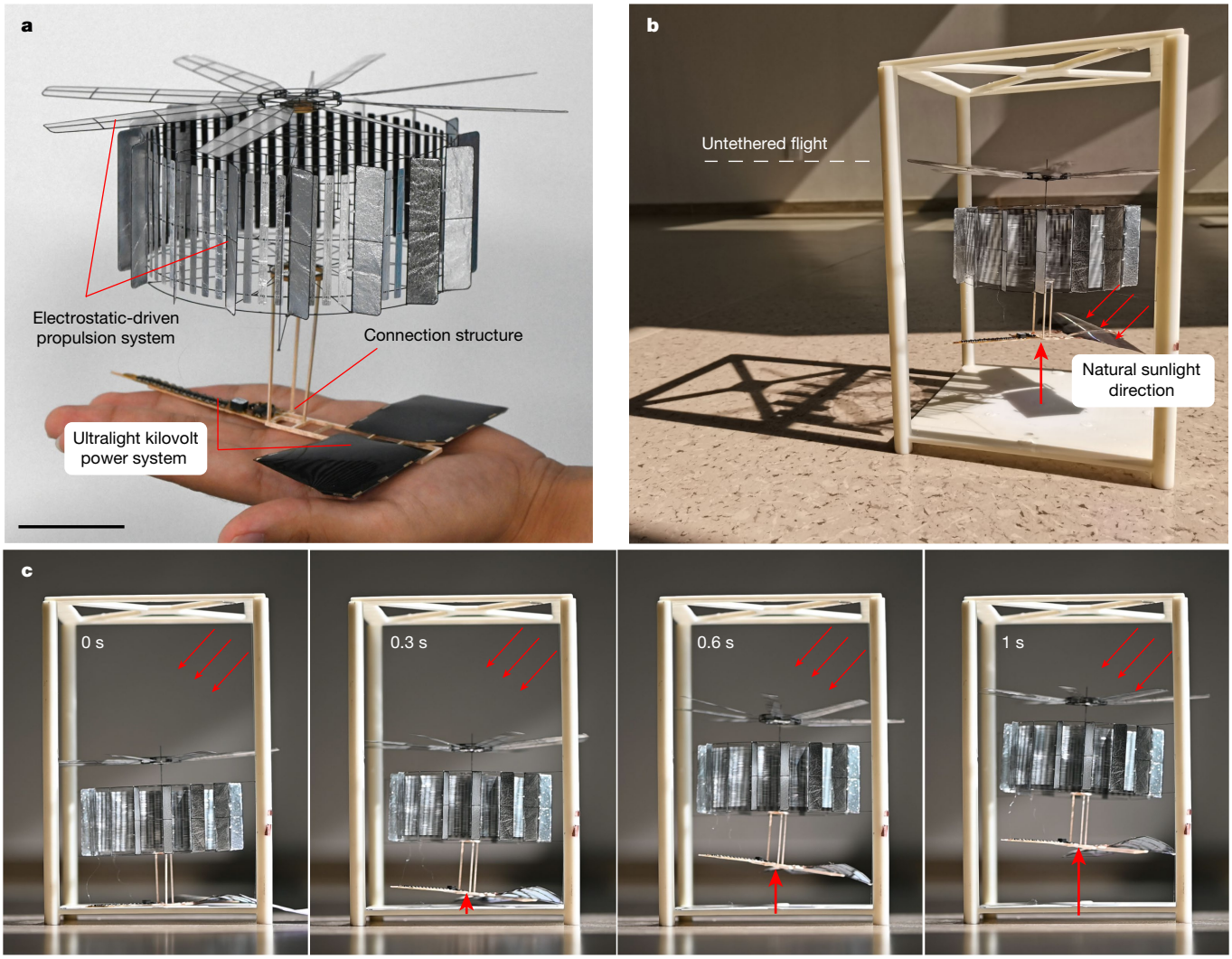

Fig. 1 | The integrated vehicle and its sunlight-powered sustained flight operation. a, The palm-sized vehicle (CoulombFly) weighs 4.21 g with a wingspan of 20 cm. It is composed of an electrostatic-driven propulsion system (1.96 g), an ultralight kilovolt power system (2.09 g) and connection structures (0.16 g), where the propulsion system consists of an electrostatic motor (1.52 g) and a propeller (0.44 g), and the power system is made up of a HVPC (1.13 g, 4.0–9.0 kV) and solar cells (0.96 g). Scale bar, 20 mm. **b**, The flying vehicle in the flight test system powered by natural sunlight with an incident angle of 48°. **c**, The process of taking off and sustained flight of the vehicle after being exposed to sunlight. The vertical red arrows represent flight altitude and the inclined red arrows represent the natural sunlight direction.

motor along with the HVPC to ensure the separation of low-voltage and high-voltage components as well as sufficient sunlight exposure. This layout also lowers the overall centre of gravity, improving the vehicle's stability.

We build a flight test system, as shown in Fig. 1b, where the flying vehicle is guided by two vertical rails to maintain its lateral position. The sunlight-powered flight test was conducted in Beijing, China, at 11:50 am during the spring. The weather was sunny with a light intensity of 920 W m^{-2} and a relative humidity of 34%. The window was open to ensure direct sunlight exposure on the solar cells at a sunlight incidence angle of 48°. As shown in Fig. 1c and Supplementary Video 1, after removing the shading board placed on the solar cells, the vehicle successfully took off within 1 s to achieve sustained flight. In the flying state, the electrostatic motor consumes 0.137 W (with a lift-to-power efficiency of 30.7 g W^{-1}), and the total system consumes 0.568 W (with a total lift-to-power efficiency of 7.6 g W^{-1}). We also conducted a long-term test (1 h), as shown in Supplementary Video 5, which illustrates that the electrostatic motor did not experience performance degradation, and the vehicle maintained sustained flight throughout the test.

Electrostatic-driven propulsion system

The core component of the propulsion system is an electrostatic motor (Fig. 2a), which has a simple structure and absence of windings[24–27]. Electrostatic motors are generally used as sensors[28] in microelectromechanical systems (MEMS) and are not applied to the propulsion of aerial vehicles. We designed an electrostatic motor to achieve high torque and low power consumption within a mass of 1.52 g. As illustrated in Fig. 2a, the electrostatic motor comprises two main components: the rotor and the stator. The rotor (marked as grey) consists of 64 blades and a pair of connecting rings. The rotor blades are made of 20-μm-thick carbon fibre sheets covered by a layer of 1-μm-thick aluminium foil, and the connecting rings are made of insulated glass fibres (0.3-mm thick). The stator consists of eight pairs of electrodes arranged in a ring pattern with alternating positive (red) and negative (blue) electrodes, all connected together by a pair of insulated rings. The electrode plates are also made of a 0.19-mm-thick carbon fibre skeleton bonded to aluminium foil (1.5-μm-thick Mylar film and 1-μm-thick aluminium film). There is an electric brush (2 mm in length) at the edge of each electrode plate for soft contact and charge transfer with the

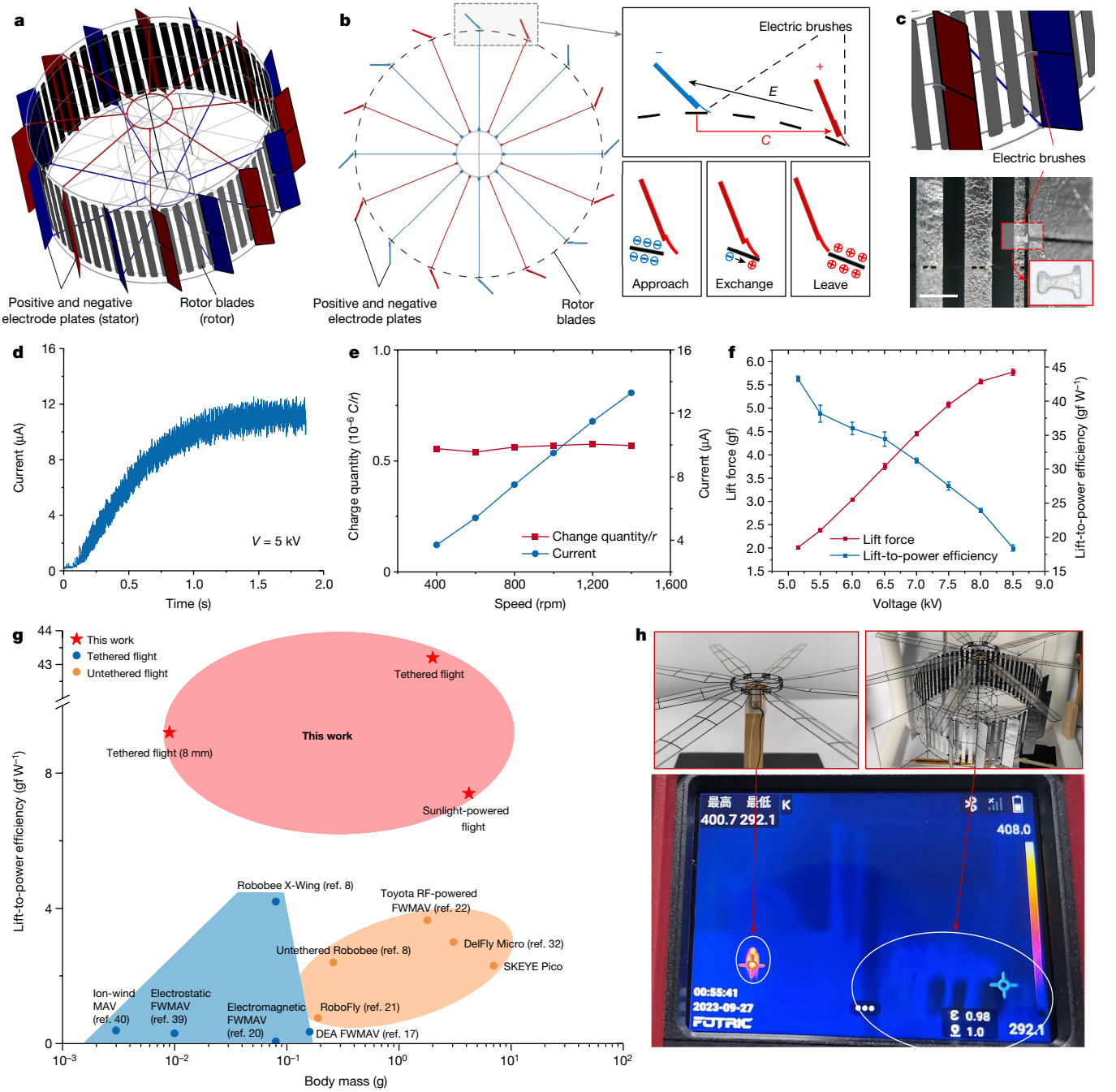

Fig. 2 | Structure design, working principle and output characteristics of the electrostatic-driven propulsion system. a, The structural design of the electrostatic motor. The red and blue parts represent the positive and negative electrode plates, and the grey parts represent the rotor blades. **b**, Schematic diagram (top view) of the electrostatic motor's working principle, showing the rotor blades' charge-transfer process between the positive and negative electrodes via electric brushes, where *C* represents the capacitor between the rotor and the next electrode plate and *E* represents the electric-field strength between the electrode plates. **c**, Detailed structure of electric brushes. The top panel shows the 3D structural design and the bottom panel is a photograph, the inset is a magnified photograph of an electric brush. Scale bar, 5 mm. **d**, The transient current curve with time after applying a d.c. voltage of 5 kV to the electrostatic motor. **e**, The average current and charge quantity per revolution (*r*) curves with the speed of the electrostatic motor under a constant voltage of 5 kV. **f**, Lift force and lift-to-power efficiency curves of the propulsion system under different applied voltages. The error bars are s.d. **g**, Lift-to-power efficiency comparison of existing ultralight aerial vehicles. Data for SKEYE Pico from https://trndlabs.com/pages/drone-academy_skeye-pico-drone. **h**, Thermal image comparison (bottom panel) between the electrostatic (top right panel) and electromagnetic (top left panel) motors during sustained flight operation. DEA, dielectric elastomer actuator; RF, radiofrequency; FWMAV, flapping-wing micro aerial vehicle.

rotator blades (see details in Fig. 2c). The brush is made of 20-μm-thick aluminium foil and cut by a laser cutting machine (Han's laser uv-3c). The positive (negative) electrodes are connected by eight carbon fibre rods marked as red (blue) for structural support and conducting electricity. The traditional bearings between the stator and rotor have been replaced with a dry friction design for weight reduction. All three-dimensional structures mentioned above are assembled from two-dimensional flat materials (such as carbon fibre sheet, glass fibre sheet and aluminium foil) cut by laser cutting technology (see details in Extended Data Fig. 4).

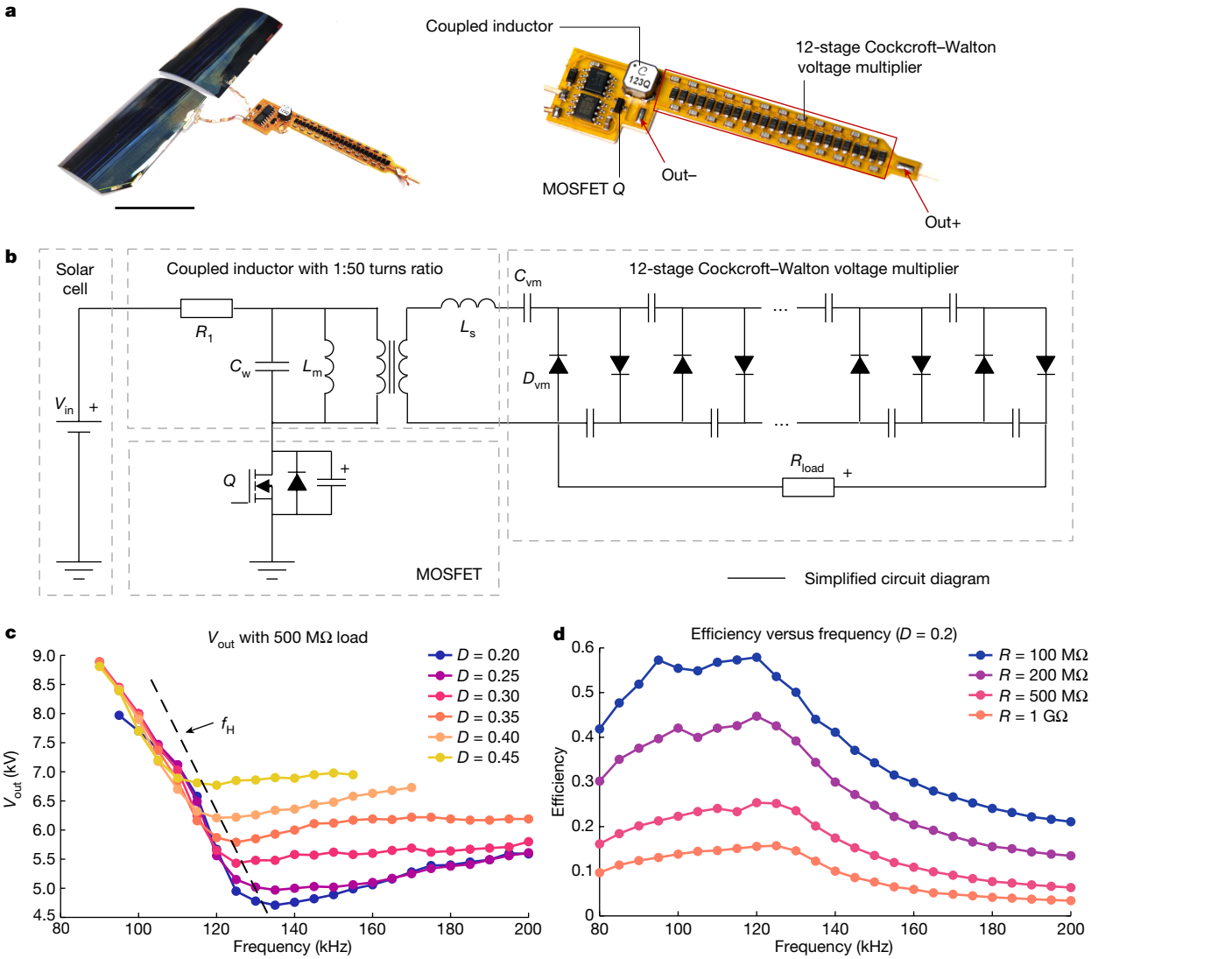

Fig. 3 | Topology and characteristic curves of the ultralight kilovolt power system. a, Photograph of the actual power system consisting of a HVPC and solar cells. Scale bar, 50 mm. **b**, Circuit design of the HVPC, consisting of a coupled inductor, a MOSFET switch and a 12-stage Cockcroft–Walton voltage multiplier, where V_{in} is the input voltage, R_1, C_w, L_m and L_s are the winding resistor, winding capacitor, magnetic inductor and secondary side leakage inductor of the coupled inductor, Q is the ideal MOSFET, C_{vm} and D_{vm} are the capacitors and diodes of the Cockcroft–Walton voltage multiplier, and R_{load} is the load resistor of the HVPC. **c**, Output voltage V_{out} curves of the HVPC with different switching frequencies with a 500-MΩ R_{load}. **d**, Power conversion efficiency curves with different load resistances powered by a 3.7 V Li-ion battery when the duty cycle is 0.2.

The working principle of the electrostatic motor is based on the charge transfer between the rotor and stator through the electric brushes. As shown in Fig. 2b, when a high d.c. voltage is applied to the stator electrodes, it forms 16 circumferentially arranged electrostatic fields (E) to drive the rotor blades. During the rotation, the rotor blades alternately pass through each positive and negative electrode and generate reciprocating charge transfer through the brushes and electrodes for continuous rotation of the electrostatic motor (Supplementary Video 2). This work uses electric brushes instead of the traditional corona effect[29,30] for charge transfer, which substantially improves the performance of electrostatic motors. Although the electric brush may cause some friction losses, it eliminates large voltage loss compared with the corona effect[31]. Figure 2d shows the transient current characteristics of the electrostatic motor, contrasting with those of conventional electromagnetic motors that generate maximum current at start-up or when stalled. Supplementary Video 3 shows that the electrostatic motor has almost zero current in a stalled state, ensuring the vehicle's safety and low power consumption in the event of foreign object interference.

Another notable feature of this electrostatic motor is its ability to maintain constant torque and self-adjust its speed in response to changing loads. As shown in Fig. 2e, when we vary the motor load while keeping the applied voltage constant, the operating speed and current will be adjusted passively to different applied loads (the blue line). The speed–current curve is almost a straight line, indicating that the operating speed is proportional to the operating current. The horizontal red line indicates that the driving torque remains constant regardless of the motor's load and speed changes.

We designed and manufactured a propeller with a radius of 100 mm and combined it with the electrostatic motor to form an electrostatic-driven propulsion system (Extended Data Fig. 2a). After conducting multiple repeated tests on propulsion systems from different production batches, the results showed that the maximum lift of the propulsion system is 5.8 g and the maximum lift-to-weight ratio is 2.9. The propulsion system's lift force, power consumption and lift-to-power efficiency characteristics are shown in Fig. 2f and Extended Data Fig. 2b. When the applied voltage increases from 5.0 kV to 8.5 kV, the power consumption increases from 0.047 W to 0.314 W,

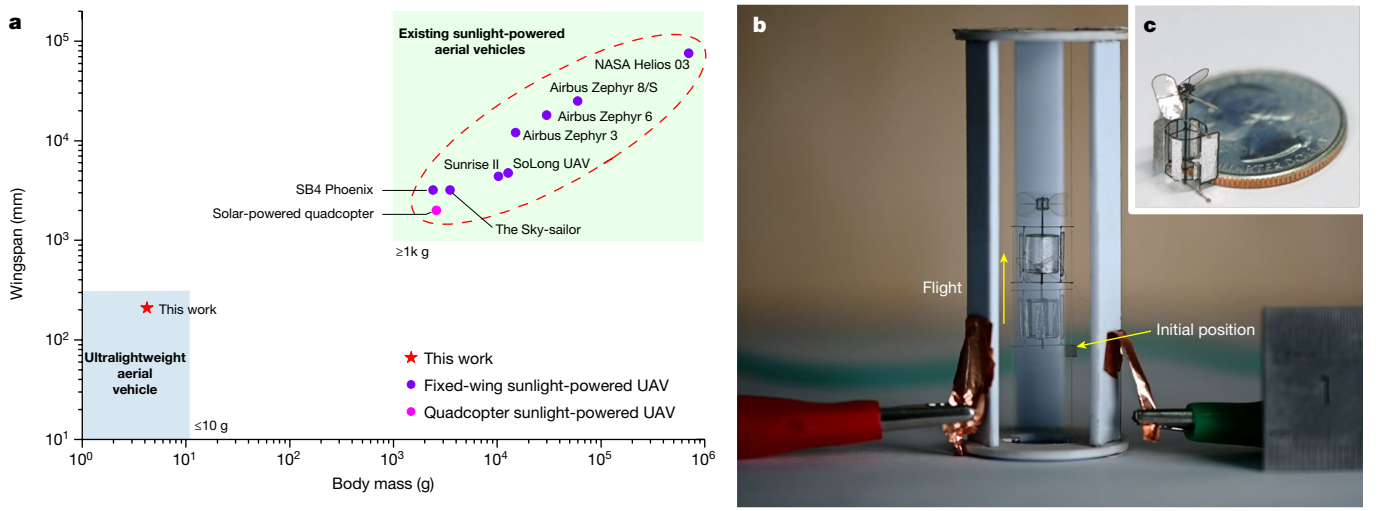

Fig. 4 | Size comparison and miniaturization of the vehicle. a, Size and mass comparison of existing sunlight-powered unmanned aerial vehicles (UAVs) with untethered flight. **b**, Tethered flight operation of a millimetre-sized prototype. **c**, Photograph of the millimetre-sized prototype (8 mm in diameter and 9 mg in mass).

while the lift-to-power efficiency of the propulsion system varies from 20.2 g W^{-1} to 43.3 g W^{-1}. According to the total lift-to-power efficiency comparison of existing ultralight aerial vehicles shown in Fig. 2g, the lift-to-power efficiency of our vehicle (7.4 g W^{-1}) is 2–3 times that of other untethered MAVs (2.3–3.7 g W^{-1}; refs. 8,21,22,32 and SKEYE Pico, https://trndlabs.com/pages/drone-academy_skeye-pico-drone). Benefiting from the characteristic of low current (9.3 μA to 36.9 μA) of the electrostatic motor, the power consumption of the electrostatic motor is 0.181 W on average and no heat is generated during the rotation. In the temperature comparison test (Fig. 2h and Supplementary Video 4), when driving the same propeller at the same rotating speed, the temperature of the electrostatic motor remained at its initial temperature after extended operation. In contrast, a traditional electromagnetic motor's temperature rose rapidly under the same load.

Ultralight kilovolt power system

An ultralight (2.09 g) kilovolt power system is designed to meet the electrostatic motor's high-voltage and low-current requirements. As shown in Fig. 3a, the power system consists of two high-power-density solar cells (SC-3TGA24-1-A, purchased from Shanghai Institute of Space Power-Sources) and a HVPC. The solar cells are made of gallium arsenide thin film, which has a high energy conversion efficiency of 30%. The size of a single solar cell is 4 cm × 6 cm, with a mass of 0.48 g and a maximum power density of 0.8 W g^{-1} (at 1 sun). We used two cells connected in series with an open-circuit voltage of 6.04 V to meet the start-up voltage (4.30 V) of the HVPC, which converts the solar cells' output voltage (4.50 V) into the operating voltage (4.0–9.0 kV) of the electrostatic motor. The HVPC is assembled on a 0.05-mm-thick polyimide flexible printed circuit board (PCB) manufactured by laser ablation (Extended Data Fig. 6 and Extended Data Table 2). The HVPC circuit weighs 1.13 g, the step-up ratio varies from 900 to 2,000, and the voltage-to-mass ratio is 7.09 kV g^{-1}, which is 55% higher than the previously lightest kilovolt high-voltage generator (4.32 kV, 951 mg)[33].

For the HVPC, a compact layout and a high voltage-to-mass ratio are essential to meet the vehicles' voltage and mass requirements. Traditional power converters based on flyback topology are frequently used for low-power applications, and their typical output voltage rarely exceeds hundreds of volts[34,35]. Moreover, a high-turns-ratio transformer may increase leakage inductances, leading to voltage and current spikes over switches, necessitating high-rated voltage components or increased losses in snubber circuits. In this work, we designed a forward-flyback converter with a 12-stage Cockcroft–Walton voltage multiplier, as depicted in Fig. 3a, which is a viable solution for high voltage gain while reducing the voltage stress of components[36–38]. The HVPC consists of a switch metal–oxide–semiconductor field-effect transistor (MOSFET), a coupled inductor with a 1:50 turns ratio, and a 12-stage Cockcroft–Walton voltage multiplier, as depicted in Fig. 3b. The HVPC can achieve high output voltage and low power with minimal components and lower mass compared with conventional topologies[33]. Utilizing the characteristic of the Cockcroft–Walton voltage multiplier, energy can be delivered to the load through the coupled inductor regardless of the state (switched on or off) of the switch in the forward-flyback topology. Unlike the conventional flyback topology, the parasitic inductors of the coupled inductor enable the absence of a separate magnetizing inductor, reducing the converter's cost, mass and size.

In practical tests, the output voltage of the HVPC varies within a range of 4–9 kV with changes in load resistance, switching frequency and duty cycle. Figure 3c depicts the converter's output voltage with different switch frequencies and duty cycles for a 500-MΩ load. It can be seen that when operating at a specific duty cycle, the output voltage of the HVPC varies with switching frequency and reaches a minimum at a particular frequency f_H. As the switching frequency decreases from f_H, the output voltage under different duty cycles increases rapidly at the same slope. Considering the reliability of the HVPC and its ability to enable high output voltage, an 86-kHz and 0.2-duty-cycle switching signal is selected, achieving an output voltage of 9.0 kV. The HVPC consumes 0.568 W (on average) to drive the electrostatic motor at the experimentally determined operating conditions for untethered flight (6.8 kV, equivalent resistance of 330 MΩ), depicting a power conversion efficiency of 24.1%. The energy conversion efficiency of the HVPC is related to the load resistance and the switching frequency, as shown in Fig. 3d. It can be seen that as the load resistance decreases from 1 GΩ to 100 MΩ, the maximum power conversion efficiency of the HVPC increases from 15% to 58%. In the future, we can improve the efficiency of HVPC by designing a minor equivalent load resistance of the electrostatic motor. In addition, when the load resistance is constant, with a specific frequency range (80 kHz to 120 kHz), the power conversion efficiency of the HVPC undergoes relatively minor changes. With a suitable range of frequency and duty cycle, we can ensure that the power conversion efficiency of the HVPC remains almost constant, as shown in Extended Data Fig. 5, allowing for a wide range of output voltage adjustments, thereby meeting the requirements for various actions such as take-off, hovering, ascent, descent and landing of the vehicles.

Size comparison and miniaturization of the vehicle

Figure 4a shows that, to our knowledge, our vehicle is currently the lightest and smallest sunlight-powered aerial vehicle compared with existing works[5]. The smallest existing work that can realize sunlight-powered sustained flight is a solar-powered quadcopter[6] (2 m in size and 2.6 kg in mass) with a power efficiency of 8.6 g W^{-1}, whereas our vehicle is about 1/10 of its size and 1/600 of its mass. It is noted that existing sunlight-powered aerial vehicles generally use electromagnetic motors and fixed-wing configurations. To achieve long endurance, previous works often adopted a rather large wingspan to provide a sufficient area for solar cells. However, this resulted in a bulky structure, and there are limitations regarding application scenarios for these vehicles. To address these problems, different types of actuator (such as piezoelectric ceramic, dielectric elastomers and linear electromagnetic) with high efficiency and low power consumption at small sizes have been presented, and several even smaller MAVs achieve untethered flight using solar cells[8,21], but they are powered by a high-power-density laser or triple sunlight (3 sun). In other words, attaining untethered, sustained flight fully powered by natural sunlight remains a considerable challenge for MAVs. This work presents an electrostatic-driven propulsion system with a high lift-to-power efficiency that is two to three times (Fig. 2g) that of traditional methods and realizes sunlight-powered sustained flight of an MAV.

To verify the possibility of further miniaturization for ultrasmall vehicles (wingspan <10 mm and mass <10 mg), we also presented the tethered flight of a miniaturized prototype (8 mm in size and 9 mg in mass) as shown in Fig. 4b,c and Supplementary Video 6. The structural composition and assembly diagram of the miniaturized vehicle are shown in Extended Data Fig. 1. The take-off rotation speed is 10,860 rpm (Reynolds number 1.2×10^3), and the maximum rotation speed is 15,650 rpm. It has an extremely low power consumption of 0.97 mW during flight, with a lift-to-power efficiency of 9.2 g W^{-1}, more than twice that of other tethered MAVs[17,20,39,40]. Manufacturing processes and vehicle stiffness are the primary factors limiting the further miniaturization and enlargement of the vehicle.

Discussion

Through a system-level design exploration, we integrate an electrostatic-driven propulsion system, an ultralight HVPC and high-power density solar cells to demonstrate sunlight-powered sustained flight of a 4.21-g ultralight aerial vehicle. The measured maximum lift of the current system is 5.8 g at a voltage of 8.5 kV, with an extra payload capacity of approximately 1.59 g to carry additional lightweight actuators, sensors and control electronics for future autonomous operation. The sunlight-powered sustained flight demonstration represents a notable milestone in developing MAVs with long flight duration. Utilizing an electrostatic-driven propulsion system for flight is an innovative and effective method in MAVs and nano aerial vehicles and provides another option for vehicle design. Our system can substantially increase the endurance of MAVs, thus expanding their potential applications in the future, such as long-distance and long-duration aerial reconnaissance.

To further reduce the size and mass of the vehicle, more system-level improvements are expected as follows. (1) Optimizing the electrostatic motor and the propeller to increase the output torque and lift efficiency. (2) Integrating solar cells with the vehicle load-bearing framework to further improve the material and energy utilization efficiency. (3) Further marching the operating point of the HVPC and solar cells to improve the energy conversion efficiency of the HVPC.

The current limitation of our work to outdoor applications is that the prototype has a single degree of freedom, no onboard control system or active control surfaces for autonomous operation, and requires vertical guide rails to maintain its lateral position. In the future, we can add damping films[41] or balance rods[42] to achieve hovering through passive stabilization. Another option would be active control: adopting multi-rotors to counteract the counter torque of the propeller.

The sudden decrease in light intensity and high humidity in the environment are considerable limitations to driving the MAV in natural sunlight conditions. For example, clouds or other obstructions in the sky can cause a sudden decrease in light intensity. For air humidity, excessively high air humidity can make the air less insulating (reducing breakdown voltage), thereby affecting the performance of the electrostatic motor. In the future, the vehicle can be powered by a combination of rechargeable batteries and solar cells, potentially enabling 24-hour flying operations. This solution can also enhance the environmental adaptability of the vehicle, allowing it to maintain flight in low-light-intensity or even no-light conditions.

Online content

Any methods, additional references, Nature Portfolio reporting summaries, source data, extended data, supplementary information, acknowledgements, peer review information; details of author contributions and competing interests; and statements of data and code availability are available at https://doi.org/10.1038/s41586-024-07609-4.

1. Floreano, D. & Wood, R. J. Science, technology and the future of small autonomous drones. *Nature* **521**, 460–466 (2015).
2. Phan, H. V. & Park, H. C. Insect-inspired, tailless, hover-capable flapping-wing robots: recent progress, challenges, and future directions. *Prog. Aerosp. Sci.* **111**, 100573 (2019).
3. Farrell Helbling, E. & Wood, R. J. A review of propulsion, power, and control architectures for insect-scale flapping-wing vehicles. *Appl. Mech. Rev.* **70**, 010801 (2018).
4. Yan, M. & Ebel, T. in *Titanium for Consumer Applications* (eds Froes, F. et al.) 91–113 (Elsevier, 2019).
5. Zhu, X., Guo, Z. & Hou, Z. Solar-powered airplanes: a historical perspective and future challenges. *Prog. Aerosp. Sci.* **71**, 36–53 (2014).
6. Goh, C. S., Kuan, J. R., Yeo, J. H., Teo, B. S. & Danner, A. A fully solar-powered quadcopter able to achieve controlled flight out of the ground effect. *Prog. Photovolt.* **27**, 869–878 (2019).
7. Boucher, R. J. Sunrise, the world's first solar-powered airplane. *J. Aircr.* **22**, 840–846 (1985).
8. Jafferis, N. T., Helbling, E. F., Karpelson, M. & Wood, R. J. Untethered flight of an insect-sized flapping-wing microscale aerial vehicle. *Nature* **570**, 491–495 (2019).
9. Kaltenbrunner, M. et al. Flexible high power-per-weight perovskite solar cells with chromium oxide–metal contacts for improved stability in air. *Nat. Mater.* **14**, 1032–1039 (2015).
10. Alvissalim, M. S. et al. Swarm quadrotor robots for telecommunication network coverage area expansion in disaster area. In *Annual Conference of the Society of Instrument and Control Engineers (SICE)* 2256–2261 (IEEE, 2012).
11. Bi, Y. C., Lan, M. L., Li, J. X., Lai, S. P. & Chen, B. A lightweight autonomous MAV for indoor search and rescue. *Asian J. Control* **21**, 1732–1744 (2019).
12. Gerdes, J. W., Gupta, S. K. & Wilkerson, S. A. A review of bird-inspired flapping wing miniature air vehicle designs. *J. Mech. Robot.* https://doi.org/10.1115/1.4005525 (2012).
13. De Croon, G., De Clercq, K., Ruijsink, R., Remes, B. & De Wagter, C. Design, aerodynamics, and vision-based control of the DelFly. *Int. J. Micro Air Veh.* **1**, 71–97 (2009).
14. Steltz, E., Seeman, M., Avadhanula, S. & Fearing, R. S. Power electronics design choice for piezoelectric microrobots. In *2006 IEEE/RSJ International Conference on Intelligent Robots and Systems* 1322–1328 (IEEE, 2007).
15. Wood, R. J. The first takeoff of a biologically inspired at-scale robotic insect. *IEEE Trans. Rob.* **24**, 341–347 (2008).
16. Graule, M. A. et al. Perching and takeoff of a robotic insect on overhangs using switchable electrostatic adhesion. *Science* **352**, 978–982 (2016).
17. Chen, Y. F. et al. Controlled flight of a microrobot powered by soft artificial muscles. *Nature* **575**, 324–329 (2019).
18. Kim, S. et al. Laser-assisted failure recovery for dielectric elastomer actuators in aerial robots. *Sci. Robot.* **8**, eadf4278 (2023).
19. Liu, Z., Yan, X., Qi, M., Zhang, X. & Lin, L. Low-voltage electromagnetic actuators for flapping-wing micro aerial vehicles. *Sens. Actuators A* **265**, 1–9 (2017).
20. Zou, Y., Zhang, W. & Zhang, Z. Liftoff of an electromagnetically driven insect-inspired flapping-wing robot. *IEEE Trans. Rob.* **32**, 1285–1289 (2016).
21. James, J., Iyer, V., Chukewad, Y., Gollakota, S. & Fuller, S. B. Liftoff of a 190 mg laser-powered aerial vehicle: the lightest wireless robot to fly. In *2018 IEEE International Conference on Robotics and Automation (ICRA)* 3587–3594 (IEEE, 2018).
22. Ozaki, T., Ohta, N., Jimbo, T. & Hamaguchi, K. A wireless radiofrequency-powered insect-scale flapping-wing aerial vehicle. *Nat. Electron.* **4**, 845–852 (2021).
23. Elkunchwar, N., Chandrasekaran, S., Iyer, V. & Fuller, S. B. Toward battery-free flight: duty cycled recharging of small drones. In *2021 IEEE/RSJ International Conference on Intelligent Robots and Systems (IROS)* 5234–5241 (IEEE, 2021).
24. Jefimenko, O. *Electrostatic Motors: Their History, Types and Principles of Operation* (Integrity Research Institute, 2010).
25. Ludois, D. C. et al. Macroscale electrostatic rotating machines and drives: a review and multiplicative gain performance strategy. *IEEE J. Emerging Sel. Top. Power Electron.* **10**, 14–34 (2020).

26. Fan, L. S., Tai, Y. C. & Muller, R. S. IC-processed electrostatic micro-motors. *Tech. Digest International Electron Devices Meeting* 666–669 (IEEE, 1988).
27. Livermore, C. et al. A high-power MEMS electric induction motor. *J. Microelectromech. Syst.* **13**, 465–471 (2004).
28. Yasseen, A. A., Mitchell, J. N., Klemic, J. F., Smith, D. A. & Mehregany, M. A rotary electrostatic micromotor 1/spl times/8 optical switch. *IEEE J. Sel. Top. Quantum Electron.* **5**, 26–32 (1999).
29. Lee, S., Kim, D., Bryant, M. D. & Ling, F. F. A micro corona motor. *Sens. Actuators A* **118**, 226–232 (2005).
30. Leng, J. et al. Design and analysis of a corona motor with a novel multi-stage structure. *J. Electrostat.* **109**, 103538 (2021).
31. Chang, J.-S., Lawless, P. A. & Yamamoto, T. Corona discharge processes. *IEEE Trans. Plasma Sci.* **19**, 1152–1166 (1991).
32. Deng, S., Percin, M. & van Oudheusden, B. Aerodynamic characterization of 'DelFly Micro' in forward flight configuration by force measurements and flow field visualization. *Procedia Eng.* **99**, 925–929 (2015).
33. Park, S., Drew, D. S., Follmer, S. & Rivas-Davila, J. Lightweight high voltage generator for untethered electroadhesive perching of micro air vehicles. *IEEE Robot. Autom. Lett.* **5**, 4485–4492 (2020).
34. Ravi, V. & Lakshminarasamma, N. Steady state voltage gain of flyback converters for high voltage low power applications. In *2016 IEEE International Conference on Power Electronics, Drives and Energy Systems (PEDES)* 1–6 (IEEE, 2016).
35. Kewei, H., Jie, L., Xiaolin, H. & Ningjun, F. Analysis and simulation of the influence of transformer parasitics to low power high voltage output flyback converter. In *2008 IEEE International Symposium on Industrial Electronics* 305–310 (IEEE, 2008).
36. Zhiguo, Z. & Lin, Z. Analysis and design of isolated flyback voltage-multiplier converter for low-voltage input and high-voltage output applications. *IET Power Electron.* **6**, 1100–1110 (2013).
37. Dall'Asta, M. S., Fuerback, V. B. & Lazzarin, T. B. DCM forward-flyback converter integrated with a 5-order Cockcroft–Walton voltage multiplier: a steady-state and resonant current analysis. In *2017 Brazilian Power Electronics Conference (COBEP)* 1–6 (IEEE, 2017).
38. Serrano-Vargas, J. A., Oliver, J. A. & Alou, P. Forward–flyback converter with Cockcroft–Walton voltage multiplier in DCM: steady-state analysis considering the parasitic capacitances to achieve the optimal valley-switching operation with 95.11% efficiency at 3 kV/1.5 W. *IEEE J. Emerg. Sel. Top. Power Electron.* **10**, 2351–2361 (2022).
39. Yan, X., Qi, M. & Lin, L. Self-lifting artificial insect wings via electrostatic flapping actuators. In *2015 28th IEEE International Conference on Micro Electro Mechanical Systems (MEMS)* 22–25 (IEEE, 2015).
40. Drew, D. S. & Pister, K. S. J. First takeoff of a flying microrobot with no moving parts. In *2017 International Conference on Manipulation, Automation and Robotics at Small Scales (MARSS)* 1–5 (IEEE, 2017).
41. Chen, N. et al. A self-rotating, single-actuated UAV with extended sensor field of view for autonomous navigation. *Sci. Robot.* **8**, eade4538 (2023).
42. Johnson, K. et al. Toward sub-gram helicopters: designing a miniaturized flybar for passive stability. In *2023 IEEE/RSJ International Conference on Intelligent Robots and Systems (IROS)* 2701–2708 (IEEE, 2023).

Publisher's note Springer Nature remains neutral with regard to jurisdictional claims in published maps and institutional affiliations.

Springer Nature or its licensor (e.g. a society or other partner) holds exclusive rights to this article under a publishing agreement with the author(s) or other rightsholder(s); author self-archiving of the accepted manuscript version of this article is solely governed by the terms of such publishing agreement and applicable law.

© The Author(s), under exclusive licence to Springer Nature Limited 2024

Methods

Vehicle design

Two key parameters must be considered when designing a sunlight-powered MAV: lift force and solar cell power. The primary reason existing MAVs cannot achieve untethered flight in natural sunlight is the insufficient power of solar cells. Owing to the vehicle payload and size limitations, the area of solar cells that MAVs can deploy is inadequate. The key to solving this problem is to improve the lift-to-power efficiency of the vehicle's propulsion system because higher lift-to-power efficiency means generating greater lift force with limited power.

The first step is to determine the size of the electrostatic motor to be designed to ensure sufficient torque (or lift force). According to the working principle of electrostatic motors, we can simplify the electrostatic torque (M_e) of the rotor to:

$$M_e = N\bar{E}qR_0 \tag{1}$$

where M_e is the electrostatic force applied to the rotor, N is the number of blades, R_0 is the radius of the rotor, $\bar{E}$ is the average electric-field strength between the electrode plates and q is the charge on a single blade. It is noted that N is positively correlated with R_0; the larger the rotor radius (R_0), the greater the number of rotor blades (N). The formula can be expressed as:

$$M_e = k_0\bar{E}qR_0^2 \tag{2}$$

where k_0 is the proportional coefficient of the number of rotor blades. From the formula, it can be seen that when the stator electrode spacing remains constant, under the condition of constant spacing between the stator electrode plates (ensure that $\bar{E}$ remains constant), the electrostatic force torque of the rotor increases rapidly with proportional enlargement. Increasing the size of the electrostatic motor is the most effective solution to give the vehicle enough lift. We made a series of electrostatic motors with different sizes and determined that a 60-mm-radius electrostatic motor can give the vehicle enough torque output (or lift). The size of the electrostatic motor determines the electrostatic torque at the macro level, which is also related to the parameters of the static and rotor. To maximize the electrostatic torque, it is also necessary to find the optimal parameter design within this size (60 mm), which will be introduced in the next section.

After determining the size of the electrostatic motor, we need to consider the lift-to-power efficiency of the vehicle. Matching the propeller with the electrostatic motor is crucial for achieving high lift-to-power efficiency and lift for the vehicle. On the basis of the basic principles and characteristics of the electrostatic motor, we know that, under constant voltage, the electrostatic force torque of the rotor is constant and independent of the speed. At the same time, the energy conversion efficiency (η) of the electrostatic motor is related to only the charge-transfer process, not the speed. Therefore, the input power (P) of the electrostatic motor is associated with the electrostatic power (P_e) of the rotor as follows:

$$P = VI = \frac{P_e}{\eta} = \frac{M_e\omega}{\eta} = \frac{2\pi M_e n}{\eta} \tag{3}$$

where V is the input voltage of the electrostatic motor, I is the input current of the electrostatic motor, η is the energy conversion efficiency of the electrostatic motor, which does not change with speed, unlike the electromagnetic motor, ω is the angular velocity of the electrostatic motor and n is the speed of the electrostatic motor. The electrostatic torque of the rotor is used to drive both the rotor and the propeller simultaneously, so M_e can be divided into two parts:

$$M_e = M_R + M_P \tag{4}$$

where M_R is the torque used to drive the rotor and M_P is the torque used to drive the propeller. When the speed is low, M_R is small, and most of the electrostatic torque of the rotor (M_e) is used to drive the propeller. Therefore, at low speeds, it can be considered that $M_e \approx M_P$.

A fixed-pitch propeller is often used for a rotorcraft. The lift-to-power efficiency of a propeller[43] can be derived from thrust T, propeller torque M_P and motor power P. According to refs. 44,45, they are expressed as:

$$T = C_T\rho\left(\frac{n}{60}\right)^2 D_P^4 \tag{5}$$

$$M_P = C_M\rho\left(\frac{n}{60}\right)^2 D_P^5 \tag{6}$$

where n is the propeller speed, D_P is the diameter of the propeller, C_T and C_M are the dimensionless thrust coefficient and torque coefficient, respectively, and ρ is air density. We can get the propeller power (P_P) and lift-to-power efficiency (σ) formula as follows:

$$P_P = 2\pi M_P n \approx 2\pi M_e n \tag{7}$$

$$\sigma = \frac{T}{P} = \frac{T}{VI} = \frac{T\eta}{2\pi M_e n} \approx \frac{T\eta}{2\pi M_P n} = \frac{\eta c_T}{2\pi c_M}\sqrt[5]{\frac{c_M\rho}{3,600M_e n^3}} \tag{8}$$

According to equation (8), it can be seen that, under the condition of ensuring a specific applied voltage and electrostatic torque (M_e), the lift-to-power efficiency (σ) is inversely proportional to the speed. We can use a large propeller to work at low speeds to improve lift-to-power efficiency.

When designing propeller parameters, we need to consider the material and manufacturing process of the propeller comprehensively. In terms of materials, we used 1.5-μm Mylar film and 250-μm carbon fibre; for the manufacturing, we bonded the Mylar film with the carbon fibre skeleton and fixed it on a curved surface, then shaped it in an oven to create a curved propeller, ensuring an excellent aerodynamic efficiency. Lastly, the aerodynamic parameters of the propeller (including pitch and installation angle) were determined based on experimental conditions and process considerations. Considering considerations such as lift force, lift efficiency, weight and the manufacturing process, we decided on a propeller with 8 straight blades, a radius of 100 mm and an installation angle of 13°. The eight-blade propeller is designed to reduce the speed of the propeller in a limited space, although it sacrifices some thrust efficiency[46]. The lift-to-power efficiency curves for four propellers of different radius when paired with the same electrostatic motor are shown in Extended Data Fig. 2c,d. The experiment shows that with the propeller size increase, although the propulsion system's speed decreases, the force-to-power efficiency substantially improves.

Electrostatic motor

An excellent structural design of the electrostatic motor is also the key to achieving flight. To our knowledge, this is the first time an electrostatic motor has been used as a critical part of the aerial propulsion system, and in the past, the electrostatic motor was relatively bulky. At the same time, there are many types of electrostatic motor structure, and the one with the best performance may not be suitable for flight. We tried many electrostatic motor structures and finally designed the one depicted in Fig. 2a, which has two advantages: lightweight and low air drag.

As depicted in Fig. 2b, when a rotor blade contacts a brush of an electrode plate, a capacitor (C) between the rotor and the next electrode plate will be formed, mainly determining the amount of charge the rotor blade can transfer each time. The charged rotor blade is subjected to electrostatic force in the electric field and moves towards the next electrode plate. When the rotor blade passes through the next electrode plate, charge exchange occurs, and the polarity of the rotor blade and

the direction of the electrostatic field change simultaneously, which ensures that the driving torque on the whole rotor remains consistent for continuous rotation of the electrostatic motor.

In equation (1), the electric-field strength ($\bar{E}$) is proportional to the voltage between the electrode plates (U_1), so adding a correction factor can be equivalent to the electric-field strength of the parallel plates. At the same time, the charge q depends on the voltage between the rotor blade and the next pole plate (U_2) and the capacitance formed between the rotor blade and the next pole plate during charge transfer (C). Therefore, equation (1) can be rewritten as:

$$M_e = N\bar{E}qR_0 = Nk_1\frac{U_1}{d}CU_2R_0 = Nk_1\frac{U_1U_2}{d}CR_0 \quad (9)$$

where k_1 is the correction factor for the electric-field strength, U_1 is the voltage between the electrode plates, U_2 is the voltage between the rotor blade and the next pole plate, d is the distance between the electrode plates, and C is the capacitance formed between the rotor blade and the next pole plate during charge transfer.

In equation (9), U_1 is the input voltage, which affects the strength of the electric field and the amount of charge on the rotor blades. The greater the U_1, the greater the strength of the electric field between the electrode plates, the more charge there is on the rotor blades. U_2 is the induced voltage generated in the corona area, which is determined by U_1 and the distance from the rotor blades to the electrode plates. If brushes are used to make soft contact between the rotor blade and the electrode plate, U_2 is equal to U_1.

As the adjacent electrode plates are not ideal parallel electrode plates, there is a correction factor k_1 for the electric-field distribution of the electrode plates, which is determined by the angle (α) and width (w) of the electrode plate. α mainly determines the direction of the electric-field strength to provide a large tangential electric field. However, if α is too large, it can easily cause air breakdown. The optimal range of α is between 30° and 60° after experimental testing. As for w, it notably influences the strength of the electric field. An electrostatic field simulation of the electric-field strength is carried out between two electrostatic motors with wide electrode plates and narrow ones. As depicted in Extended Data Fig. 3b, the electric-field strength is higher in the vicinity of the narrow electrode plates, resulting in an uneven electric-field distribution, a lower breakdown voltage and a lower electric-field strength in the area far from the electrode plates through which the rotor blades pass, while a wide electrode plate can make the electric-field strength more uniform. The experiment (depicted in Extended Data Fig. 3a) indicates that the electrostatic motor with a wide electrode plate (3.8 mm in width) operates under a higher applied voltage to achieve a higher rotation speed compared with that with a narrow electrode plate (0.2 mm in width).

As a result, we designed a prototype of the electrostatic motor with a radius of 60 mm, a height of 55 mm, 8 pairs of electrodes whose inclination angle and width are 45° and 11 mm, and an operating voltage of 2.5–8.5 kV. Most parts of the electrostatic motor are two-dimensional structures assembled into a three-dimensional electrostatic motor. The processing and assembly of the parts are depicted in Extended Data Fig. 4. Owing to the weak rigidity of most two-dimensional structures, preventing deformation during the assembly process is a challenge.

We analysed the performance of the electrostatic motor through a series of bench tests. Tests have shown that the operating voltage range of the electrostatic motor is 2.5–8.5 kV. The electrostatic motor can move slowly at a voltage of 2.5 kV, the minimum starting voltage of the electrostatic motor. The speed of the electrostatic motor increases as the voltage increases, and when the voltage exceeds 8.5 kV, there is a filamentous sound of ion wind, occasionally accompanied by slight discharge. The current of the electrostatic motor can be divided into two parts: one part is formed by the charge transfer of the rotor blades and the other is formed by the movement of ions in the air. When the voltage has not reached the discharge voltage, the current of the electrostatic motor is mainly formed by the charge transfer of the rotor blades, and the current formed by the movement of ions in the air is very weak. At this time, the energy conversion efficiency is high. When the voltage is too high, ion wind or discharge forms most of the current; therefore, the electrostatic motor should operate at a voltage lower than the voltage that produces ion wind.

There will be a humidity effect on the actuation strategy of the electrostatic motor. The extent to which humidity affects the performance varies for different parameters of the electrostatic motor. Taking the electrostatic motor used in our take-off test as an example, we found that performance remains relatively good at around 45% relative humidity, starts to decline when the relative humidity goes above 45%, and decreases by around 20–30% at relative humidity levels above 55%. This is because the air becomes less insulating in more humid conditions, which leads to a decrease in breakdown voltage.

Electronics

The two purchased thin-film solar cells in our prototype (depicted in Fig. 3a) are made of gallium arsenide with an energy conversion efficiency over 30%, a mass of 0.48 g and a size of 4 mm × 6 mm. The thin-film solar cell uses polyimide as the substrate with bending stress, so we built a lightweight wood frame and connected the two solar cells, thus flattening the solar cells a bit.

Placing solar cells on the top of a vehicle is the most ideal choice as it allows for ample exposure to sunlight. However, the top of the vehicle is occupied by the propeller, a rotating component, making it quite challenging to place the solar cells there. Therefore, the solar cells and HVPC can be placed only underneath the vehicle, lowering the vehicle's centre of gravity and enhancing the structural stability. We consider both the solar incidence angle and the connecting frame mass to determine the optimal value of the distance between the solar cells and the electrostatic motor. From the perspective of connecting frame mass, the smaller the distance, the better; however, considering the solar incidence angle, this distance should ensure that the vehicle body does not block the light to the solar cells. On the basis of calculations, the angle of sunlight incidence around noon during the flight test was approximately 48°, so the distance we choose for the prototype is 48 mm.

Existing topologies for the HVPC are generally bulky and heavy, unsuitable for MAVs. We want to reduce the HVPC mass as much as possible while maintaining a relatively high output voltage. There are multiple aspects, such as component selection and circuit design, where we can reduce the total mass of the HVPC.

Circuit design. To achieve an ultrahigh step-up ratio, conventional topologies often use a half-bridge or full-bridge inverter to convert the input d.c. voltage to a.c. and then use a transformer or coupled inductor with a high turns ratio to amplify the a.c. voltage. Finally, a Dickson or a Cockcroft–Walton voltage multiplier with fewer stages rectifies the amplified a.c. voltage and further amplifies it. A half-bridge or full-bridge inverter generally requires four or more components to achieve the inversion function, with a maximum voltage gain of two. Furthermore, as mentioned earlier, high-turns-ratio coupling inductors are often bulky owing to higher winding-to-winding isolation voltage, and higher input a.c. voltages will further increase the voltage stress on the capacitors and diodes in the voltage multiplier.

In our work, considering the presence of parasitic parameters such as magnetizing inductor and winding capacitance in the practical coupled inductors (depicted in Fig. 3b), using a forward-flyback converter with a 12-stage Cockcroft–Walton voltage multiplier can reduce the number of components used on the primary side and control signals on the switch (MOSFET). A control signal on the gate of MOSFET controls the switch. The magnetizing inductor L_m resonates with the parasitic capacitance C_{oss} of the switch and capacitances of the Cockcroft–Walton voltage

multiplier on the secondary side of the coupled inductor, converting the 4.5-V d.c. to a 16-V a.c. (peak to peak) on the primary side of the coupled inductor. The 16-V a.c. is amplified to 800-V a.c. (peak to peak), delivered to the secondary side, and further amplified and rectified by the Cockcroft–Walton voltage multiplier, generating a 9-kV d.c. output voltage. It can operate near the resonant frequency to achieve a higher gain for the conversion (depicted in Extended Data Fig. 5). Considering the voltage stress of the voltage multiplier, the shortcoming of the Dickson voltage multiplier is that the capacitor at the last stage (closest to the output port; farthest from the input port as depicted in Fig. 3) needs to withstand voltage stress that is equivalent to the output voltage, resulting in the bulky package of the capacitor and the diode.

Components selection. In general, the packaging and mass of electronics are influenced by their electrical characteristics. The packaging of the coupling inductor is influenced by factors such as the winding-to-winding isolation voltage and saturation current. It is neither deserved to select a coupling inductor with a larger turns ratio from the same series nor necessary to select a coupling inductor with higher winding-to-winding isolation voltage. The applied maximum d.c. voltage and capacitance value generally affect the packaging and mass of capacitors. The higher the applied d.c. voltage and capacitance value, the larger the packaging and the greater the mass of the capacitor. The packaging and mass of diodes increase with the increasing reverse voltage. The breakdown voltage and the continuous drain current affect the switch's packaging. The larger the breakdown voltage and the continuous drain current, the larger the package of the switch generally. Moreover, using a flexible printed circuit board enables a great reduction of the total mass of HVPC.

To minimize the complexity and facilitate rapid prototyping, the electronics design utilizes commercial off-the-shelf devices whenever possible. We chose the coupled inductor LPR6235-123Q to match the desired turns ratio and inductance. For this work, the transformer had a primary-to-secondary turns ratio of 1:50. A capacitor (rated as 4.7 μF, GRM188C81E475KE11D) provided sufficient charge at the input during system operation. A complete list of components and their mass distribution is provided in Extended Data Table 2.

To satisfy the insulation requirements, we designed a single-sided printed circuit board, which eliminated the need for vias. The circuit was fabricated using a direct-write photolithography on copper-clad polyimide. All components were then hand-positioned and attached using reflow soldering. A complete fabrication process can be seen in Extended Data Fig. 6.

We chose the microcontroller STC15W104 to generate the square waveform, which is able to control the on–off state of the MOSFET (BSS316N). The voltage stress that we apply to the MOSFET achieves a peak voltage of 16 V in a period. The voltage then multiplies by a factor of 50 and 12, and the output voltage V_{out} is finally formed.

Circuit test. During the test, the circuit is connected to the solar cells on the input port and the electrostatic motor on the output port. When the electrostatic motor is operated at the conditions used for flight (approximately 6.7 kV and 20.1 μA), the electrostatic motor consumes 0.135 W (IV). Supplied by the solar cell (V_{in} = 4.50 V), the electronics consume an average of 0.568 W (P_{in}) when driving the vehicle at these conditions (measured on the screen of the power source PEAKMETER PM3005B). This includes an average power of 0.065 W that is consumed by the microcontroller (P_{mc}) to generate pulses. Thus, the efficiency of the drive electronics is $IV/(P_{in} - P_{mc}) \approx 25\%$. The primary loss mechanisms in this circuit, which contribute to the decreased efficiency, are switching losses and losses in the magnetic components and diodes.

The efficiency of the HVPC varies with the load resistance, working frequency and duty cycle. The energy of the HVPC is mainly composed of the active power of load resistance, the switching and conduction loss of the MOSFET, the reactive power of the parasitic inductors and capacitances in the coupled inductor and diodes, and the inherent power consumption of the signal circuit. When the load resistance increases and the output power decreases, the proportion of other power consumption will increase, decreasing the power conversion efficiency. Extended Data Fig. 5 illustrates the output voltage and power conversion efficiency curves with different load resistances, switching frequencies and duty cycles when a 3.7-V lithium-ion battery powers the HVPC. The output voltage of HVPC decreases with decreasing load resistance, resulting in lower voltage stress and power consumption on magnetic components, capacitances and diodes, higher power transferred to the load resistance, and higher efficiency. When the load resistance decreases to under 100 MΩ, the energy conversion efficiency can reach more than 55%. Besides, it can be observed that as the frequency decreases from f_H, the output voltage rapidly increases at the same slope and reaches a maximum at frequency f_L. As the duty cycle increases, f_L and f_H decrease, and the minimum and maximum output voltages increase accordingly. The power-conversion-efficiency curves depict that when the switching frequency is between f_L and f_H, the power conversion efficiency of the HVPC is at its highest and almost unaffected. By comparing the power conversion efficiency at different duty cycles, it can be seen that the highest efficiency is consistently within the range of f_L and f_H, and it is barely affected by the duty cycle. Therefore, with a suitable range of frequency and duty cycle, we can ensure that the power conversion efficiency of the HVPC remains constant, allowing for a wide range of output voltage adjustments, thereby meeting the requirements for actions such as take-off, hovering, ascent, descent and landing of the vehicles. The subsequent optimization will focus on three aspects: (1) how to further increase the output voltage of the HVPC, (2) how to reduce the equivalent resistance of the electrostatic motor, and (3) how to optimize the efficiency of the HVPC under light load and high resistance.

Propulsion system testing

To ensure enough lift for untethered flight and to determine the maximum payload capacity, we tested the flight performance of the electrostatic motor propulsion system (electrostatic motor and propeller). We measured the lift while recording the voltage and current of the electrostatic motor. As the Reynolds number of the prototype for flight test is calculated to be 4.4×10^4, such a small Reynolds number will lead to highly unsteady flow fields around the propellers in terms of velocity fluctuations, thus leading to uncertainty in the force measurements. To avoid this problem, we used the method of suspending weights to measure the lift force, which can demonstrate the vehicle's load-carrying capacity more intuitively.

We also conducted durability experiments on the electrostatic motor to verify that the electrostatic motor does not suffer performance degradation during operation (Supplementary Video 5). In the experiment, we conducted a durability test on the vehicle for one hour, and the vehicle remained in sustained flight throughout the test. The subsequent experimental results show that the electrostatic motor can still work normally, and the performance remains stable after one hour of continuous operation. This experiment demonstrates electrostatic motors' excellent stability and durability, providing a foundation for the future development of long-endurance MAVs.

Flight test

The flight test was scheduled on a sunny morning with good air quality and high visibility. The test was conducted indoors (as shown in Fig. 1b,c), and the light intensity in the room was measured as 920 W m^{-2}, with sunlight coming in through the window. During the test, the angle of incidence of the sunlight was 48°; the light intensity would be higher in the summer. The vehicle successfully took off by placing the test platform in the sunlight (Supplementary Video 1) and removing the shading board placed on top of the solar cells to block the light. Therefore, it was verified that the vehicle can fly in natural sunlight. In general,

outdoor lighting is stronger than indoor lighting because of the diffuse reflection in outdoor lighting, enabling better vehicle performance.

Further data on the vehicle were recorded during the flight. We connected an ammeter and a voltmeter to the low-voltage terminal of the HVPC and measured a current of 0.126 A and a voltage of 4.50 V (0.576 W). As the resistance of the high-voltage probe (the device for measuring the high-voltage applied, with a 500-MΩ resistor) is comparable to the equivalent resistance of the electrostatic motor (300–400 MΩ), the voltage at the high-voltage terminal of the HVPC could not be measured directly by the oscilloscope and the high-voltage probe. We use the equivalent method to measure the voltage at both ends of the electrostatic motor when it is flying, that is, we use a high-voltage power supply (KIKUSUI TOS5101) to put the vehicle in the flying state and measure the current of the vehicle through an electrometer (Keithley Model 6514) then record the voltage and current in this state, which are 6.8 kV and 20.1 μA (0.136 W), respectively. It is noted that although the output voltage is high, the power and current are extremely low, causing almost no damage to the human body. At the same time, we also measured the rotating speed during flight, which was as low as 625 rpm and resulted in almost no noise.

Data availability

All data generated or analysed for this paper are included in the published article, Methods and Supplementary Information. Original videos and sensor data are available from the corresponding authors on reasonable request.

43. Quan, Q. *Introduction to Multicopter Design and Control* (Springer 2017).
44. Shastry, A. K., Kothari, M. & Abhishek, A. Generalized flight dynamic model of quadrotor using hybrid blade element momentum theory. *J. Aircr.* **55**, 2162–2168 (2018).
45. Xiao, K., Meng, Y., Dai, X., Zhang, H. & Quan, Q. A lifting wing fixed on multirotor UAVs for long flight ranges. In *2021 International Conference on Unmanned Aircraft Systems (ICUAS)* 1605–1610 (IEEE, 2021).
46. Harrington, A. M. *Optimal Propulsion System Design for A Micro Quad Rotor* (Univ. Maryland, 2011).

Acknowledgements This work is supported by the National Natural Science Foundation of China (grant number 52272384). Any opinions, findings, conclusions or recommendations expressed in this material are those of the authors and do not necessarily reflect the views of the National Natural Science Foundation of China.

Author contributions M.Q. and X.Y. proposed and designed the research. W.S. and J.P. designed and built the ultralight MAV. W.S., R.M. and J.W. conducted the experimental work on the electrostatic-driven propulsion system. J.P. and J. Li conducted the experimental work on the ultralight kilovolt power system. Z.L. and J. Leng contributed to the modelling and data analysis. W.S., J.P. and M.Q. drafted the paper. All authors provided feedback.

Competing interests The authors declare no competing interests.

Additional information
Supplementary information The online version contains supplementary material available at https://doi.org/10.1038/s41586-024-07609-4.

Correspondence and requests for materials should be addressed to Xiaojun Yan or Mingjing Qi.

Peer review information *Nature* thanks the anonymous reviewers for their contribution to the peer review of this work. Peer reviewer reports are available.

Reprints and permissions information is available at http://www.nature.com/reprints.

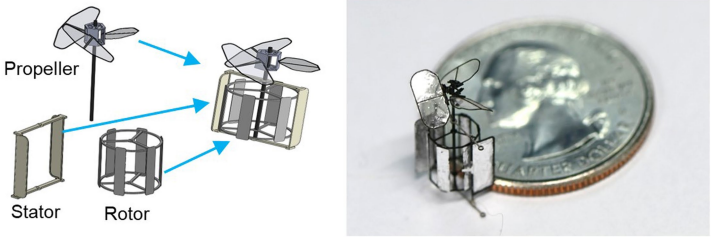

Extended Data Fig. 1 | The structural composition and assembly diagram of the miniaturized prototype. It can be seen that the vehicle has a very simple structure, making it suitable for further miniaturization.

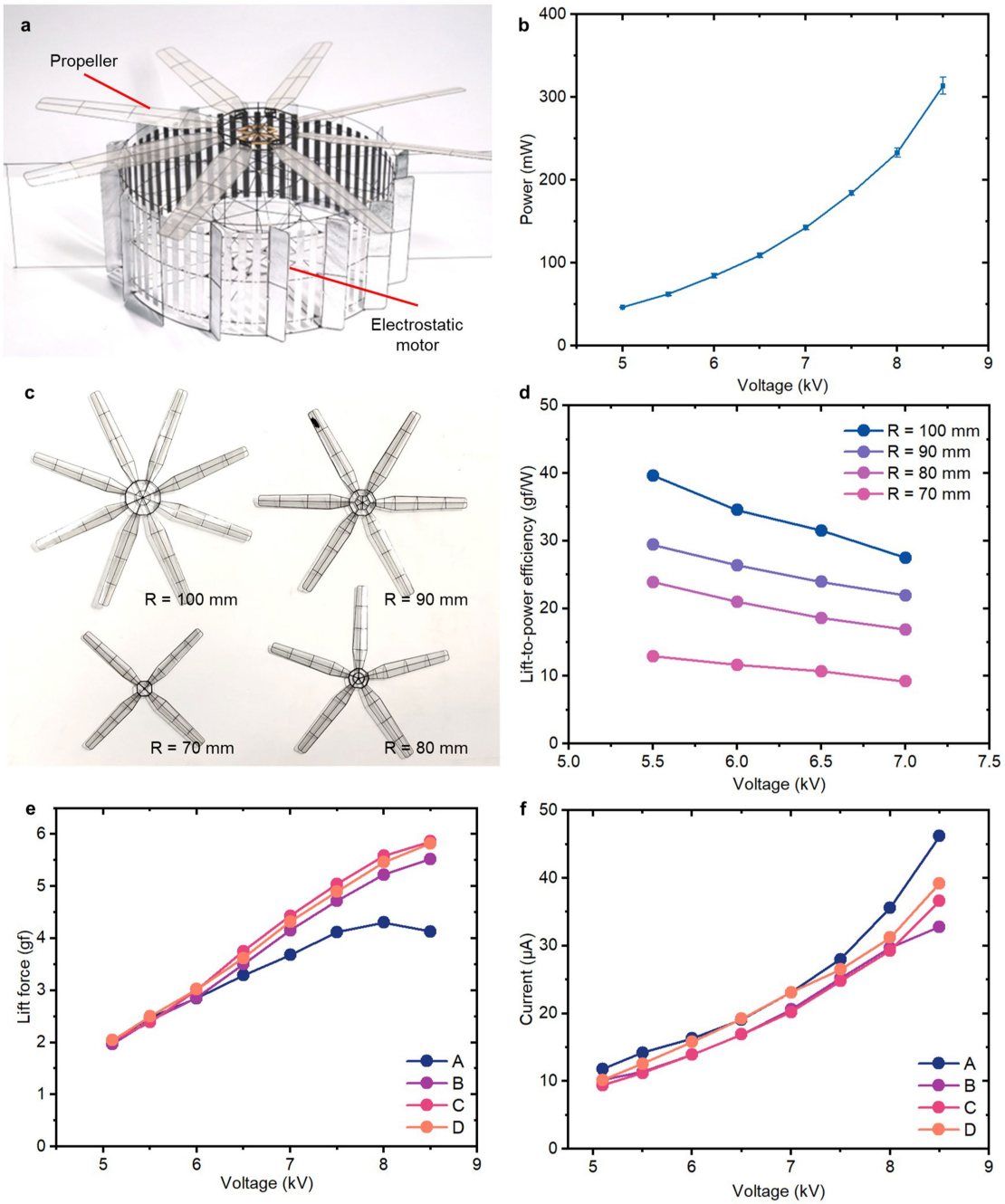

Extended Data Fig. 2 | Characteristics of the electrostatic-driven propulsion system. a, System photo (an electrostatic motor and a propeller, 1.96 g in mass). **b**, Power consumption concerning applied high DC voltages, with error bars defined in s.d. **c**-**d**, The lift-to-power efficiency characteristics of the propulsion system with four different propellers. **e**-**f**, The lift and current curves of propulsion systems from different production batches (A, B, C, D) under different applied voltages.

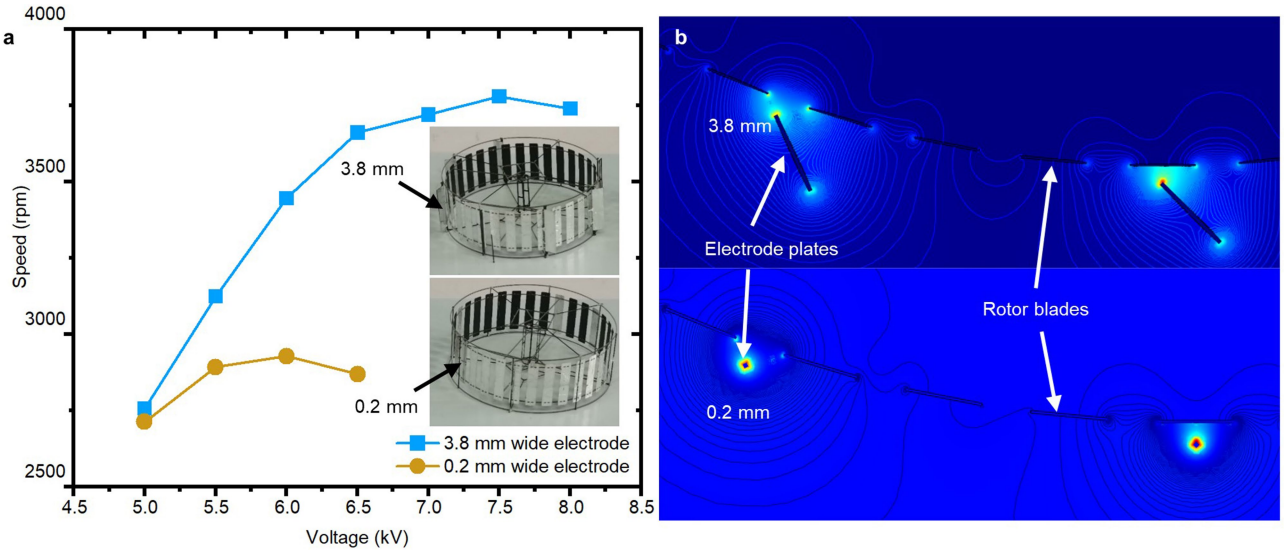

Extended Data Fig. 3 | Experiment and simulation for the electrostatic motor. a, Voltage-speed curves of electrostatic motors with 0.2 mm width and 3.8 mm width electrode plates. It can be seen that the wide electrode configuration outperforms the narrow electrode configuration. Meanwhile, the rotational speed of the narrow electrode configuration has reached its peak at 6 kV, and the electrostatic motor shows a slight discharge at this voltage, which indicates that the electric field strength to break through the air has been reached. **b**, Two-dimensional simulation for the electrostatic field of the two electrode configurations. It can be seen that the electrostatic field strength of the wide electrode configuration is consistently higher throughout the entire rotation area (as indicated by the darker color). In contrast, although obtaining a higher electrostatic field strength near the electrodes, the narrow electrode configuration suffers a rapid decline as the distance from the electrodes increases, leading to an overall driving effect that is inferior to that of the wide electrode configuration.

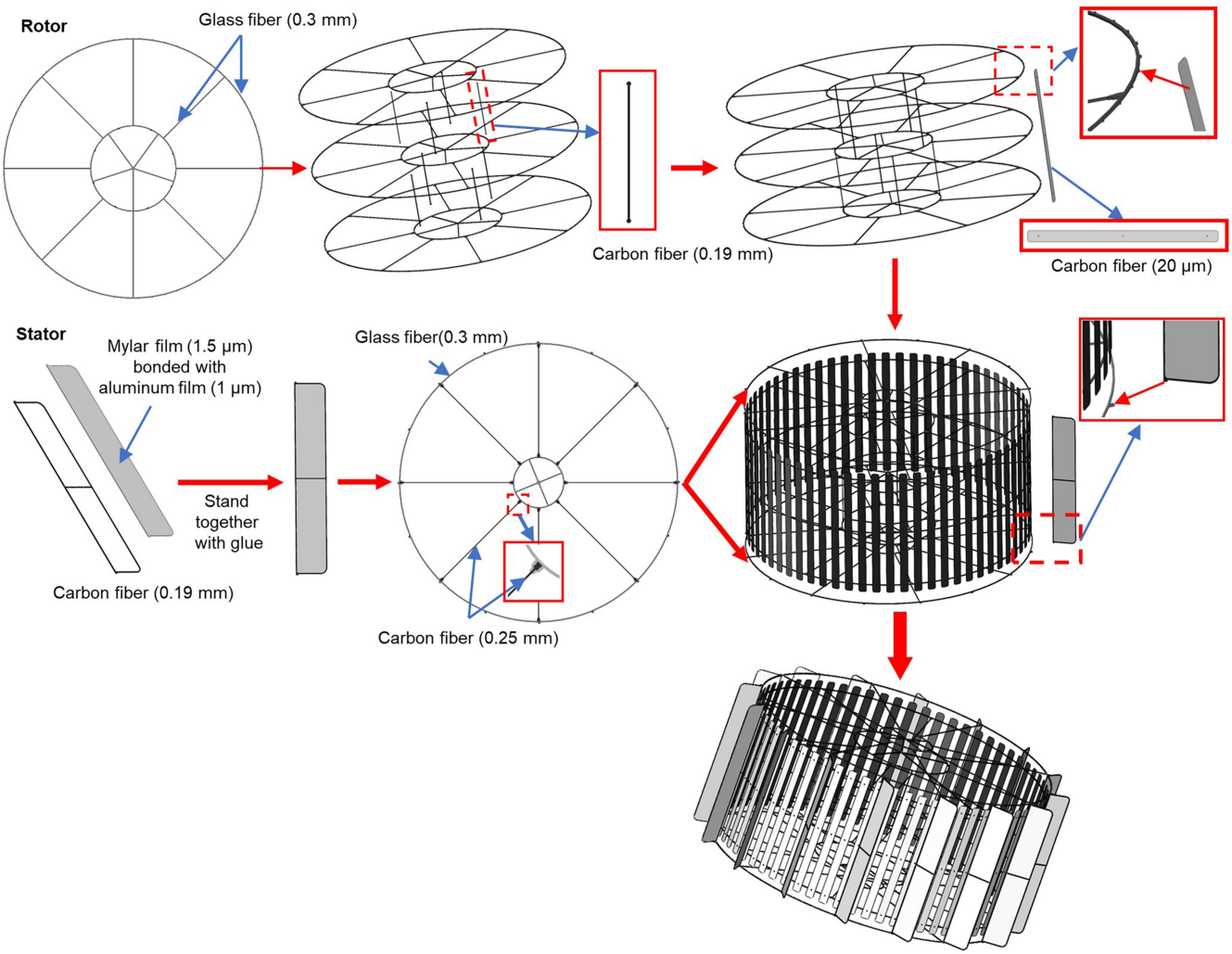

Extended Data Fig. 4 | Processing and assembly of electrostatic motors. The electrostatic motor is mainly assembled into a three-dimensional structure with two-dimensional components.

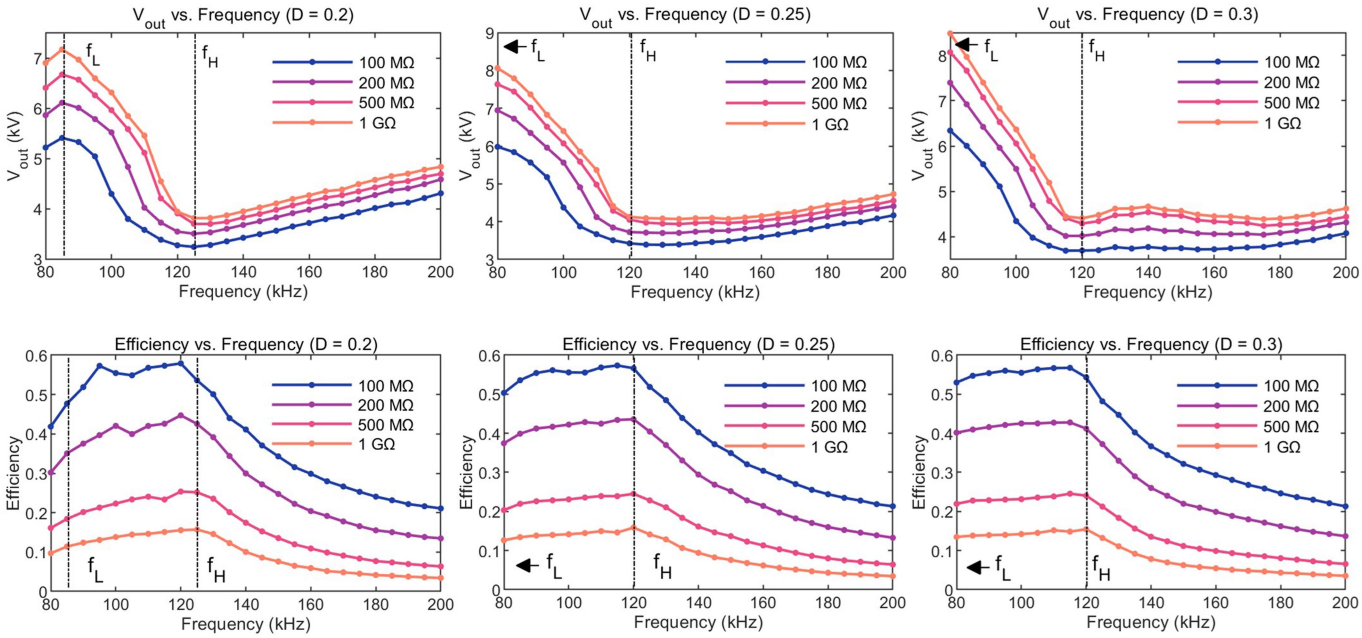

Extended Data Fig. 5 | Detailed characteristics of the high-voltage power converter. The relationship between circuit characteristics and switching frequency, duty cycle, and load resistance when the input voltage is 3.7 V. A 3.7 V Li-ion battery powers the HVPC and supplies high output voltage for different resistances (100 MΩ, 200 MΩ, 500 MΩ and 1 GΩ). The current through the load resistance is measured, the output voltage is calculated by the equation $U = IR$, the output power is calculated by $P_{out} = I^2R$. With a suitable range of frequency and duty cycle, we can ensure that the power conversion efficiency of the HVPC remains constant, allowing for a wide range of output voltage adjustments.

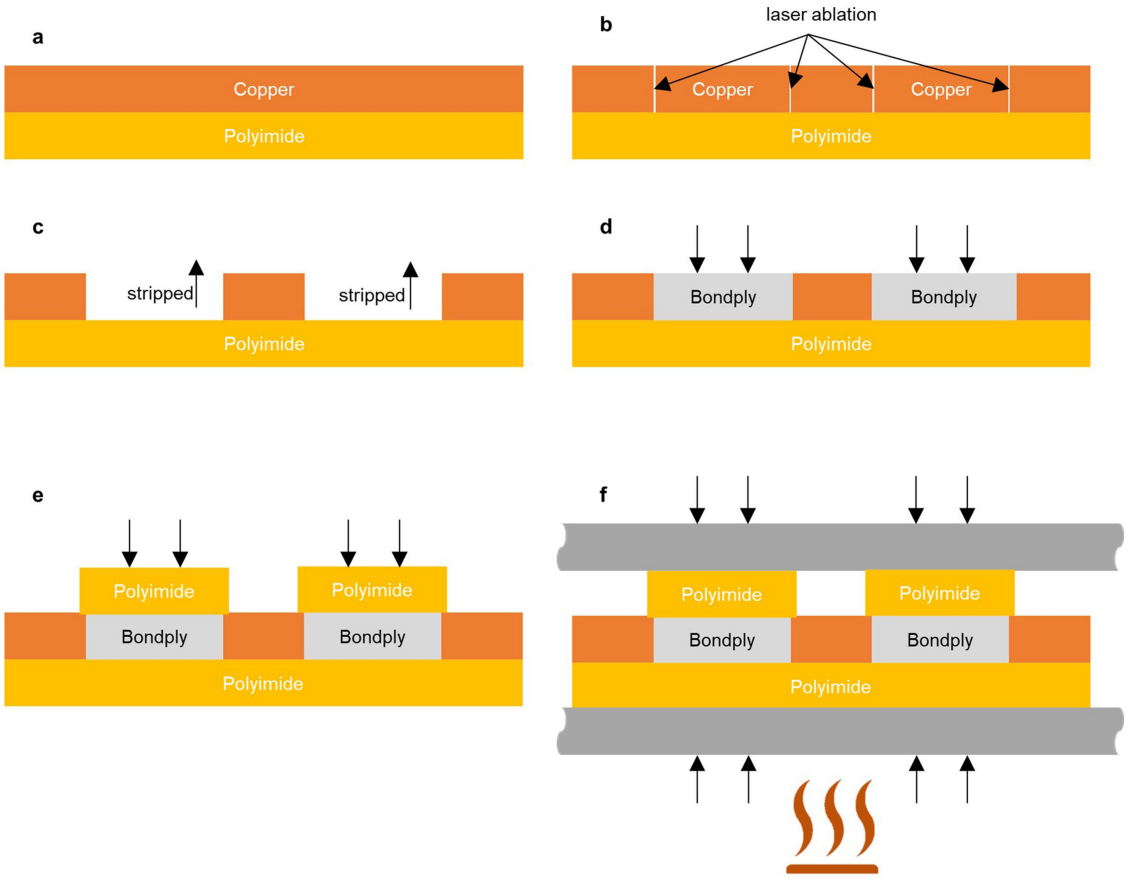

Extended Data Fig. 6 | Fabrication process of flexible PCB for the ultra-light kilovolt power system. a, Attach copper foil to the polyimide film. **b**, Use laser cutting to create the desired circuit traces without damaging the underlying polyimide film. **c**, Remove excess copper foil. **d**, Place adhesive patches. **e**, Cover the top layer with polyimide containing holes in the shape of solder pads. **f**, Apply external pressure to compress the layers and heat them at high temperature for 2 h.

Extended Data Table 1 | Main parameters for the vehicle components during flight operation

Component name		Total Mass (g)	Main Parameters
Electrostatic-driven propulsion system	Electrostatic motor	1.52	Operating voltage: 6.8 kV Operating current: 20.1 μA
	Propeller	0.44	Rotation speed: 625 rpm Lift force: 4.21 g
Ultra-light kilovolt power system	HVPC	1.13	Step-up ratio: 1511 Power conversion efficiency: 24.1 %
	Solar cells	0.96	Power density: 0.8 W/g

Extended Data Table 2 | Main parameters for the HVPC components

Name	Manufacturer / Product No.	Parts Count	Mass per count (mg)	Total Mass (mg)	Main Parameter
Transformer U_1	Coilcraft / LPR6235-123Q	1	480	480	1 : 50
Capacitor C_{vm}	KEMET / C0603V102KDRAC7867	24	5.9	141.6	1 nF, 0603
Diode D_{vm}	ROHM / RFU02VSM8STR	24	5.4	129.6	800 V
MOSFET Q_1	Infineon / BSS316NH6327	1	4	4	30 V,1.4 A
MCU	STC / STC15W104	1	76.4	76.4	-
Capacitor C_{in}	muRata / GRM188C81E475KE11D	1	5.8	5.8	4.7 μF, 0603
Gate Driver	ONSEMI / ADP3110AKRZ-RL	1	69.5	69.5	
Diode D_{BST}	SMC Diode Solutions / 1N5819W	1	10.1	10.1	
Capacitor C_{BST}	muRata / GRM188R72A104KA01D	1	5.8	5.8	100 nF, 0603
Unoccupied flex PCB	-	1	78.6	78.6	-
etc.	-	-	-	127.6	-
sum	-	-	-	1129	-